A Thesis

On

Effect of two different dopants on structural and optical properties of bismuth vanadate

Submitted in partial fulfillment of requirement for the award of Degree of Master of Technology (M. Tech.)

In

MATERIALS AND METALLURGICAL ENGINEERING

Submitted by:

Rupanjit Kaur Grewal
(601102008)

Under the Supervision of

Dr. Kulvir Singh
(Professor and Head)

School of Physics and Material Science
Thapar University
Patiala- 147004
INDIA

July 2013

CERTIFICATE

This is to certify that **Ms. RUPANJIT KAUR GREWAL, Roll No. 601102008** has worked on this thesis report entitled **"Effect of two different dopants on structural and optical properties of bismuth vanadate"** as a partial fulfillment for award of the degree of MASTER OF TECHNOLOGY in Materials and Metallurgical Engineering. I certify that the matter embodied in this report is of the candidate's own record and not submitted to any other university in any part or full form for the award of such kind of a degree.

(Dr. Kulvir Singh)
Professor and Head
School of Physics and Material Science
Thapar University
Patiala- 147004

Countersigned by:

(Dr. Kulvir Singh)
Professor and Head
School of Physics and Material Science
Thapar University, Patiala

(Dr. S.K. Mohapatra)
Dean of Academic Affairs
Thapar University, Patiala

ACKNOWLEDGEMENT

Apart from the efforts of me, the success of any project depends largely on the encouragement and guidelines of many others. I take this opportunity to express my gratitude to the people who have been instrumental in the successful completion of this thesis.

Firstly, I would like to express my deepest appreciation to my guide **Dr. Kulvir Singh, Professor and Head, School of Physics and Material Sciences, Thapar University, Patiala.** He has the attitude and the substance of a genius. He continually and convincingly conveyed a spirit of adventure in regard to research, and an excitement in teaching. Without his guidance and persistent help this dissertation would not have been possible.

I would like to thank **Dr. O.P. Pandey** and **Dr. B. N. Chudasama** for their valuable assistance and incentive.

I give my special gratitude to **Ms. Samita Thakur** whose contribution and encouragement helped me to coordinate my thesis. I owe my sincere thanks to her for her diligence and consistent adjuration for the successful completion of my work.

I am also grateful to **Ms. Sakshi Gupta** and **Mr. Satwinder Singh** and all other research scholars for the valuable information in their respective field. They never hesitated in educating me in completing this task through various stages.

I am thankful to SAIF center, Panjab University, Chandigarh for XRD measurements and FT-IR measurements. I also owe my appreciation to Mr. Bhupinder Singh and Mr. Rohit, research scholars at School of Chemistry and Bio-chemistry, Thapar University, Patiala for UV-Visible Spectroscopy.

I am also grateful to my friends Mr. Chetan Singh, Mr. Rajwant Singh, Mr. Amit Kumar, Mr. Ravi and Mr. Davinder Singh for their whole-souled reliance.

In the end, I acknowledge with a deep sense of reverence, my gratitude towards my parents and brother, who have always supported me morally.

Any omission of this brief acknowledgement does not mean lack of gratitude.

(Rupanjit Kaur Grewal)

PREFACE

The $Bi_{4-x}Pb_xV_2O_{11-\delta}$ and $Bi_4V_{2-x}Al_xO_{11-\delta}$ ($0.1 \leq x \leq 0.4$) samples were synthesized by solid state reaction method. All the samples were characterized by X-ray Diffraction (XRD) for phase identification. The XRD patterns were also refined by Rietveld Refinement to confirm the symmetry of formed phases. Further, the samples were studied for Fourier Transform Infrared Spectroscopy (FT-IR) and UV-Visible Spectroscopy for the structural and optical properties. The band gap of all the samples lies in semiconducting range. The lowest band gap of 1.66 eV is observed for $Bi_4V_{1.6}Al_{0.4}O_{11-\delta}$ among all the studied samples.

“Dedicated to my parents”

TABLE OF CONTENTS

LIST OF FIGURES

LIST OF TABLES

CHAPTER 1

INTRODUCTION

1.1 BISMUTH BASED COMPOUNDS

Bismuth based compounds are multifunctional materials which can be used in oxygen sensors, oxygen separation membranes, intermediate temperature solid oxide fuel cells and in photocatalytic reactors. The properties of these compounds are highly dependent on the processing conditions and degree of ordering and disordering in the system which further depends upon the presence of impurities and defects in the system [1]. Several methods have been adopted to engineer raw materials with better properties such as using solid solution, metal or nonmetal doping and even composites of bismuth vanadate with other materials. The final goal is to make useful, inexpensive, and non-toxic new materials which will have profound impact on science and technology.

1.2 BISMUTH OXIDE PHASES

A number of different compounds exist in binary Bi-O system, where the oxidation state of bismuth varies from +2 to +5. In a simplified description, these compounds may be considered as BiO, Bi_2O_3, Bi_2O_4 and Bi_2O_5 [1, 2]. Several modifications are found for BiO and Bi_2O_3. Since oxidation and reduction processes are relatively easy in bismuth based compounds so high concentrations of specified charge defects are typical for all bismuth based compounds which lead to form various ordered structures. Bismuth oxide forms two thermodynamically stable

polymorphic states, namely one being monoclinic α phase and the other fcc δ- phase. The α → δ transition occurs at 705 to 740 °C. Cooling down of high temperature δ - phase is accompanied by formation of an intermediate γ- and β- phase. These phases are quite unstable but γ- phase exhibits maximum conductivity. To stabilize the γ- phase many dopants are being used. Among various studied bismuth based oxides, δ - and γ- phases can be easily obtained in Bi_2O_3 - V_2O_5 system. This property makes these materials important among all the bismuth based compounds [3].

1.3 BISMUTH VANADATE

Since its discovery by *Abraham et al.* in 1988, the Bi_2O_3-V_2O_5 system has fascinated researchers with its peculiar properties. Its properties such as conductivity, polar, optical, oxygen separation membranes and photo-catalysts see their potential applicability in many scientific as well as technological fields such as, in gas sensors, catalysts, solid - state electrolytes and as electrode materials for lithium rechargeable batteries and pyroelectric detectors [4, 5, 6].

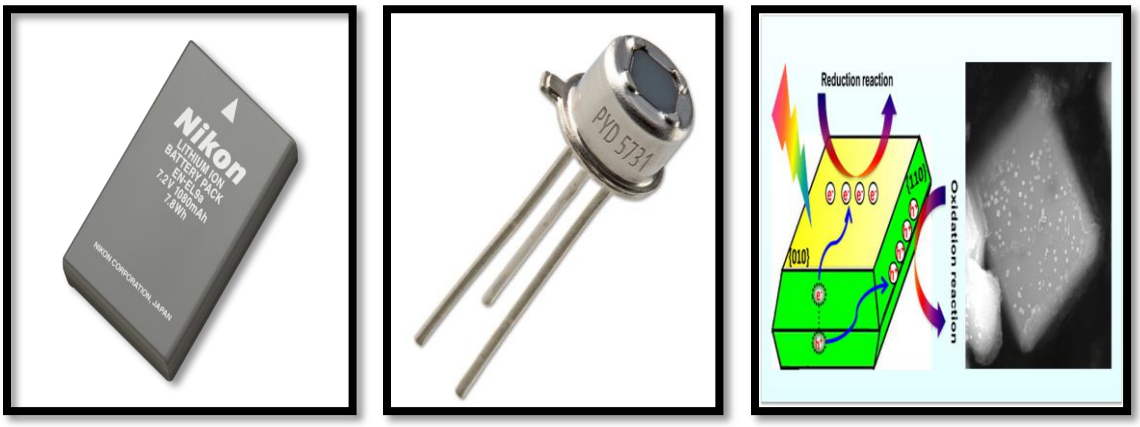

Fig 1.1: Bismuth vanadate used (from left to right) in rechargeable lithium batteries [7], pyroelectric detectors [8], and as a catalyst [9].

These systems are highly studied for these ferroelectric and conducting properties. Among the various phases of these compounds doped $Bi_4V_2O_{11-\delta}$ (BIMEVOX) and Bi_2VO_4 are also studied for their optical properties.

1.4. STRUCTURAL ASPECTS

From structural point of view, bismuth vanadate is formulated as $(Bi_2O_2)^{2+}$ $(VO_{3.5}\square_{0.5})^{2-}$, where □ represents oxide ion vacancies, $Bi_4V_2O_{11-\delta}$ can hence be considered to be analogous to α-Bi_2WO_6, n is equals to 1 for the first member of Aurivillius family of oxides i.e. $Bi_4V_2O_{11-\delta}$ with intrinsic oxygen vacancies [10, 11]. A detailed description of the structure is given below:

1.4.1. AURIVILLIUS STRUCTURES

Aurivillius in 1949 reported for the first time the Aurivillius structure [12, 13]. The generalized form is (Bi_2O_3) $(A_{m-1}B_mO_{3m+1})$. Here the metal A is in coordination number of 12, B is in 6 and m is the number of BO_6 octahedra stacked along the direction perpendicular to the sheets. From structural point of view, they consist of alternate $(Bi_2O_2)^{2+}$ shells and perovskite like $(A_{m-1}B_mO_{3m+1})$ layers. The Bi $6s^2$ lone pairs are stereochemically active and point to vacant sites between four corner sharing vanadium polyhedral in the vanadate layers. The bismuthate layers sandwich the vanadate layers with lone pair orbitals pointing directly towards each other through the vacant sites [14, 15]. The outcome of this type of geometry lies in the electronic configuration of Bi^{3+} cation which is, [Xe] $4f^{14}5d^{10}6s^2$. Here, $6s^2$ lone pair is responsible for the high polarisability of this cation and its stereochemical activity.

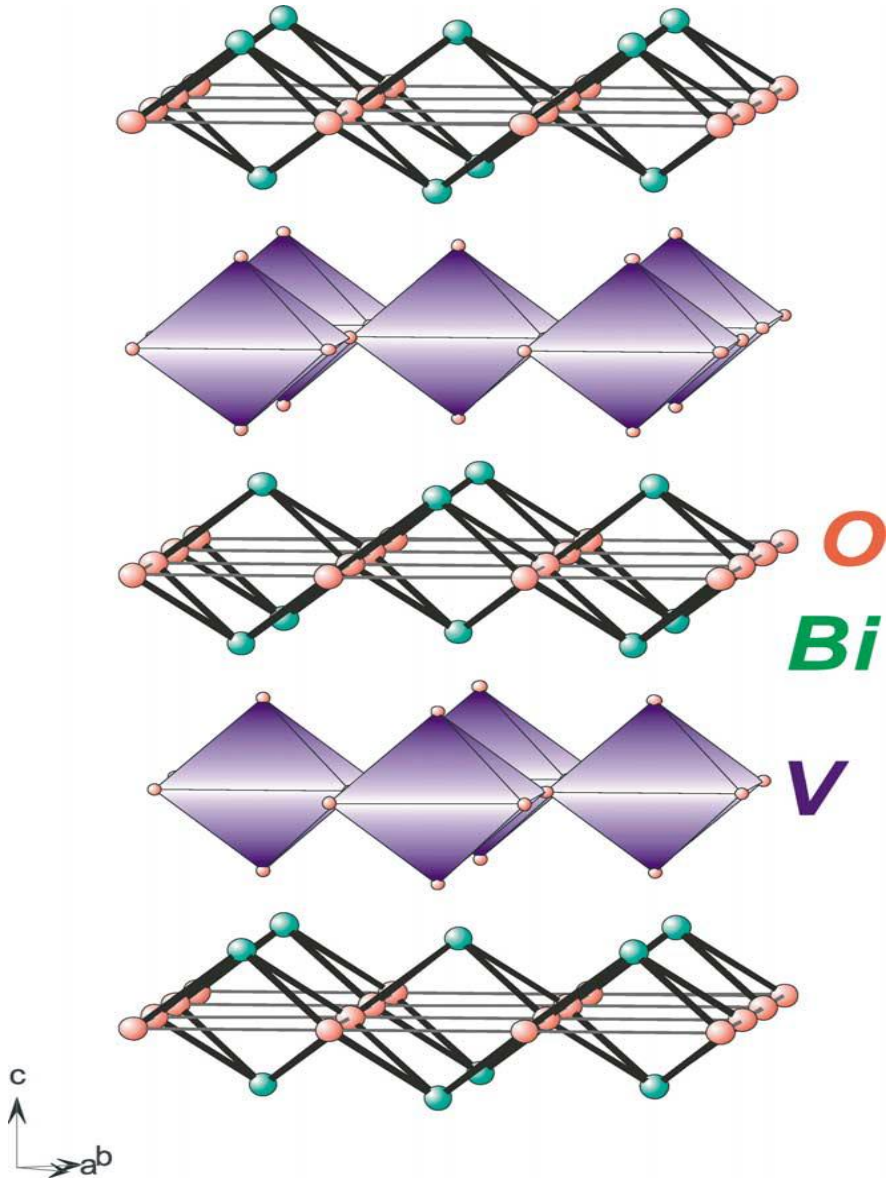

Fig 1.2: Arrangement of Bi, V, and O in bismuth vanadate structure [16].

The oxide ion conductors of this family can be classified into two groups:

- Materials based on $Bi_4V_2O_{11}$ ($Bi_2VO_{5.5}$) or (Bi_2O_2) - $[VO_{3.5}\square_{0.5}]$ which contain intrinsic oxygen vacancy and also form the parent compound for BIMEVOX. The $[Bi_2O_2]_n^{2+n}$ layers exhibit Bi in a square pyramidal coordination with four Bi–O bonds of an approximate bond

length of 2.3 Å. These are obtained by doping into the vanadium site by aliovalent or isovalent metallic cations [17].

- ❖ Materials in which extrinsic oxygen vacancies are placed by doping at A or B sites by cations of lower valence state.

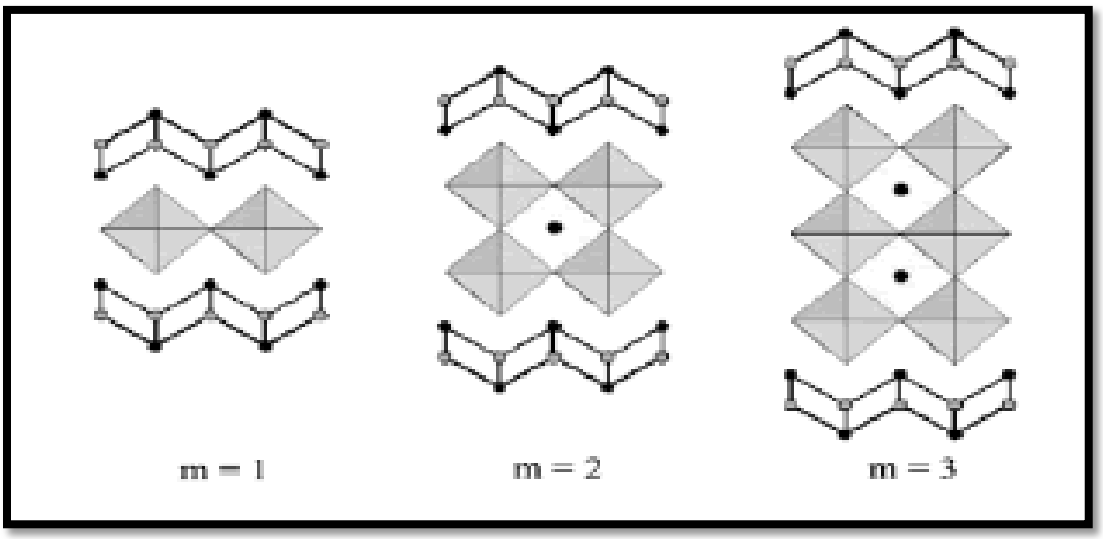

Fig 1.3: Aurivillius structure with varying m values [18].

Nowadays, atomistic simulation techniques are broadly utilized in studying the structures of the complex materials [19]. With an application point of view, these materials are particularly suited in probing. For particular, migration of ions in oxide anion conductors at an atomic scale, and have a triumphant application in fluorite, perovskite, brownmillerite- based oxides displaying intriguing anionic conductivity.

1.4.2. POLYMORPHS OF BISMUTH VANADATE

The parent compound of bismuth vanadate has a characteristic layered structure and exhibits three polymorphs:

a.) α- monoclinic (from room temperature to 430 ^{0}C).

b.) β- orthorhombic (between 470 and 570 ^{0}C).

c.) γ- tetragonal (above 570 ^{0}C up to its melting point of 870 ^{0}C).

These polymorphs can be described in mean orthorhombic unit cell with a_m = 5.5 Å, b_m = 5.6 Å, c_m = 15.3 Å. The γ- phase is described by tetragonal symmetry [19, 20]. With decreasing temperature, the symmetry decreases and β and α polymorphs are characterized by superlattice reflections. $6a_m$ superstructure is observed for α- phase and $2a_m$ for β- phase. The Bi-O layer formulated as $(Bi_2O_2)^{2+}$ exhibits Bi in a square pyramidal coordination. The asymmetric coordination geometry by bismuth results from stereochemical activity of the non-bonding Bi $6s^2$ lone pairs. The V-O layer is composed of VO_6 octahedrons that contain oxygen vacancies to preserve electroneutrality [21]. The V-O layer described as $(VO_{3.5}\square_{0.5})^{2-}$, where vanadium is pentavalent and □ denotes a randomly distributed oxygen vacancy. The β- and α- phases are characterized by the ordering of oxygen vacancies in the V-O layer.

1.5 PROPERTIES OF BISMUTH VANADATE

1.5.1 CONDUCTIVITY

Bismuth based compounds are oxygen ion conductors. The highly polarized bismuth cations accommodate oxygen disordering within the structure and thus, promote oxygen ion mobility. Solid solutions based on γ-$Bi_4V_2O_{11}$ stabilized by Ni and Cu substitution exhibit ionic conductivity of 0.2 S/cm with activation energy of 0.2 eV. But a drastic drop in the performance is noticed during γ → β and β → α transitions. The conductivity is only 0.01 Scm^{-1} at 500 ^{0}C in β domain with an activation energy of 1 eV and 10^{-5} Scm^{-1} at 300 ^{0}C in the α domain with an

activation energy of 0.6 eV. The drop in electrical performance observed for this compound is related to the crystal structure of each polymorph. The conductive properties of the materials can be controlled by partial substitution on vanadium site in parent compound of $Bi_4V_2O_{11-\delta}$. The **cation valency** which acts as a dopant modifies the anionic vacancy rate, and this influences the connectivity and symmetry of the polyhedral inside the perovskite layer which leads to increase conductivity in the system [21, 22]. A lot of research has been going on in the field of solid oxide fuel cell, and bismuth vanadate is seen as a promising compound as an electrolyte due to its property of high ion conduction.

1.5.2 OXIDE SEPARATION MEMBRANES

As it is known that bismuth vanadate belongs to the Aurivillius family. The arrangement of alternate layers of vanadate and bismuth containing oxygen vacancies, favor the oxygen ion mobility. As compared to its high ionic conductivity at temperatures as low as 600 ^{0}C, the electronic conduction rather shows a decline. Such low conductivity does not favor the semi-permeability to oxygen. So, Bismuth vanadate materials were used as electrolyte as Ceramic Oxygen Generator (COG) to parcel very pure oxygen from feeding to the delivering side [23]. Now, under imposed polarization, the material was able to covert itself reversibly and dynamically from electrolyte to electrode, which led to the formulation of a new concept of COG. In other words, the ability of bismuth vanadate to reduce and re-oxidize easily expounds their superior properties as auto-adaptive membranes for ceramic oxygen generators.

1.5.3 POLAR PROPERTIES

The bismuth vanadate compound is starred for its polar properties, i.e., dielectric, ferroelectric and pyroelectric properties at room temperature. The synthesis mechanism, morphology and size of the crystal plays critical role in determining their properties.

The studies regarding the ferroelectric thin films have drawn attention worldwide in applications, such as, non-volatile memory, microelectric-mechanical systems, infrared detectors, electro-optical switches, integrated devices, etc. From this application point of view, bismuth layered compounds are considered high-handed in comparison to lead zirconium titanate. This is due to the better fatigue properties of bismuth vanadium oxide based compounds. The other reason follows as that the Curie temperature of these materials is relatively high. It is also explained that in the Aurivillius family with the general formula of ($Bi_2A_{n-1}M_nO_{3n+3}$) the dielectric constant decreases with dropping numbers of n layers [24].

Due to the impressive dielectric properties, it is observed that grain-oriented ceramics of Aurivillius family oxides have gained immense interest in the piezoelectric applications. The piezolecetric and ferroelectric properties of high density and large degree of grain oriented ceramics are reported to be close to single crystals.

1.5.4 OPTICAL PROPERTIES

Bismuth vanadate also shows visible light driven photocatalytic properties. These are also used as photocatalysts in water splitting and oxidative decomposition of organic contamination under visible light irradiation. Bi^{3+} has a favorable $6s^2$ lone pair which is responsible for the low band gap values of these compounds. Even V^{5+} possesses the same electronic configuration as Ti^{4+},

Zr^{4+} and other ions, so bismuth vanadate exhibits satisfactory results a photocatalysts as comparison to titanium containing oxides [25]. In the next chapter, the literature review related to the optical and structural properties of doped and undoped bismuth vanadate is given.

CHAPTER 2

LITERATURE REVIEW

Joubert et al. [26] for the first time deduced the monoclinic structure of α- $Bi_4V_2O_{11}$ as seen from the XRD patterns. The true cell arises from a six-fold commensurate modulation of the orthorhombic mean cell along c_M monoclinic axis, but because of the weakness of the intensity of some diffraction lines due to the six-fold superstructure, only three-fold was investigated. However, α- $Bi_4V_2O_{11}$ is structurally related to the parent Aurillius prototype. They also explained that one-dimensional modulation depends on oxygen long-range ordering and could be viewed as resulting from coupled valence modulations.

Varma et al. [27] explained that single crystals of $Bi_2VO_{5.5}$ (BiV) had the ferroelectric Curie temperature (446 °C) which was confirmed by dielectric, pyroelectric, specific heat and hysteresis loop studies. The dielectric and specific heat data was obtained well beyond 446 °C confirmed that BiV had undergone another crystallographic transition at 553 °C.

Varma et al. [28] studied dielectric properties and microstructural characteristics of ferroelectric bismuth vanadate ($Bi_2VO_{5.5}$) ceramics. Microstructural studies indicated the presence of ferroelectric 90^0 domain patterns on the surface and in the bulk of the coarse-grained ceramics. The dielectric constant and the loss tangent both at room temperature and in the vicinity of the Curie temperature were found to increase with increasing grain size. The Curie temperature (451 °C) was found to shift slightly (by about -266 °C) towards higher temperatures as the grain

size increased (7-25 gm). The magnitude of the dielectric anomaly around 451 °C was found to be higher for coarse-grained ceramics.

Ramasesha et al. [29] studied the dielectric properties of single crystals and ceramics of $Bi_2VO_{5.5}$ and found that decrease in dielectric constant and loss with increase in pressure. However, the rate of decrease of the dielectric constant in the case of partially grain oriented ceramic was higher than that of the single crystal and conventionally synthesized ceramic. The decrease in dielectric constant with increase in pressure was attributed to the decrease in ionic polarization as a consequence of the decrease in interionic distances.

Varma et al. [30] examined the ceramics obtained from quenching melts of pre-reacted polycrystalline $Bi_2V_{5.5}$ that exhibited grain orientation (~ 55%). Microstructural studies showed ferroelectric domains. These post-annealed ceramics possessed dielectric anisotropies of about 1:1.2 at 26 °C and 1:4.3 in the vicinity of the Curie temperature (~ 456 °C) between the directions parallel and perpendicular to the quenching direction. The dielectric constants of the samples, which were obtained by quenching the melts, were found to be higher than that of the post-annealed ceramics. Furthermore, electrically poled and thermally cycled samples of both as-quenched and post-annealed exhibited ferroelectric hysteresis loops at 26 °C.

Greenblatt et al. [31] showed that solid solutions with fluorite-type, fcc, rhombohedral, tetragonal and layer structures based on Bi_2O, were excellent candidates for use as solid electrolytes and electrodes in electrochemical devices and that they were applicable at much lower temperatures than devices with stabilized zirconia. They claimed that mixed conductors based on bismuth oxide solid solutions represented an independent branch of compounds which were potentially useful as a general class of electrode materials.

Zhou et al. [32] studies showed that the structures of α-$Bi_4V_2O_{11}$ and $Bi_6V_3O_{16}$ were closely related to each other and both were derived from γ-$Bi_4V_2O_{11}$ with Bi_2O_2 layers partially depressed in an ordered manner, forming various superstructures and implying a location of oxygen vacancies in the Bi_2O_2 layers. These results necessitated a reconsideration of the mechanism of ionic conductivity in these materials.

Effects of various preparation parameters on vanadium reduction in $Bi_4V_2O_{11-\delta}$ have been studied by *Abrahams et al.* [33], and found that the amount of vanadium reduction increases drastically when rapidly quenched. Whereas, when the same samples are slowly cooled, the oxidation occurs. The band gap studies confirmed the higher conductivity at low temperatures and the NMR studies showed consistence with the presence of distorted octahedral and tetrahedral coordination of vanadium.

Xia et al. [34] studied piezoelectric properties of Pb-based ferroelectric ceramics. The results showed that these ceramics all had good piezoelectric properties near the morphotropic phase boundary. After thermal annealing, there were apparent improvements in the piezoelectric and dielectric properties and this phenomenon was attributed to the extrinsic contributions of the domain walls movement. The research showed that relaxor ferroelectric ceramics systems have good piezoelectric properties near the morphotropic phase boundary. d_{33} ~ 500 to 600 pC/N, K_p ~ 50 to 0%, d_{31} ~ 210 to -230 pC/N were achieved in thermally annealed PMN-PT. PNN-PT and PZN-BT-PT relaxor-based ceramic system. Thus, these materials were considered hopeful candidates for actuator applications.

Tabata et al. [35] studied thin films of $Bi_2VO_{5.5}$ and showed that these films had smooth surface morphology with atomically flat terraces and steps of 4 Å in height. The ferroelectric

characterization showed a spontaneous polarization of 2.2 μC/cm^2 and a coercive field (E_c) of 22 kV/cm. Also, the leakage current obtained was about 5 X 10^{-6}A/cm^2 at a drive voltage of ±2 V.

Vannier et al. [36] resolved the crystal structure of α- $Bi_4V_2O_{11}$ in A2 space group. The unit cell with measurements of a = 16.59 Å, b = 5.61 Å, c = 15.27 Å, γ = 90.260^0. It was built upon $[Bi_2O_2]^{2-}$ layers spaced with vanadium - oxygen slabs where the vanadium atoms exhibited three different oxygen environments. The main characteristic of these V - O slabs is a well-defined diametric unit with two trigonal bipyramids sharing one edge and connected to two VO tetrahedral. These rigid blocks extended along [100] and were spaced with a disordered area where different V - O trigonal bipyramids were interconnected. A possible scheme to explain the actual $6a_m$ superlattice was then proposed.

Kant et al. [37] studied series of $Bi_4V_{2-x}Al_xO_{11-\delta}$ ($0 \leq x \leq 0.4$) and showed that the conductivity measurement data exhibited a higher ionic conductivity for the sample doped with aluminum for the composition x = 0.2 as compared with other doped samples of the same series. Since the grain size and its phase distribution influence the conductivity to a great extent, the sintering parameter for the sample x = 0.2 was varied between 750 and 825 ^{0}C in an interval of 25 ^{0}C. The Arrhenius plots clearly indicated the various slope changes, which were in agreement with the phase transitions that occurred in these samples.

Varma et al. [38] showed that the polarization hysteresis (P versus E) studies on the BVO thin films at 26.85 ^{0}C confirmed the remnant polarization (Pr) and coercive field (Ec) to be 5.6 μC/cm^2 and 113 kV/cm, respectively. The same was corroborated via the capacitance–voltage measurements. A strong low frequency dielectric dispersion (LFDD) was found to exist in these films, which was ascribed to the presence of the ionized space charge carriers such as oxygen ion

vacancies and interfacial polarization. The room temperature dielectric constant and the loss (D) at 100 kHz were 233 and 0.07, respectively. The thermal activation energy for the relaxation process of the ionized space charge carriers was 0.85 eV. The frequency characteristics of BVO thin films under study showed universal dynamic response that was proposed by Jonscher for the systems associated with quasi-free charges.

Kant et al. [39] studied a new BIMEVOX series in which V^{5+} was substituted with trivalent cation Al^{3+}. γ-phase was stabilized when the substituted in the range of $0.2 \leq x \leq 0.4$ in $Bi_4V_{2-x}Al_xO_{11-\delta}$ compound. The highest ionic conductivity was found for the $Bi_4V_{1.8}Al_{0.2}O_{11-\delta}$ compounds with a sintering temperature of 800 ^{0}C as compared to samples sintered at 750, 775 and 825 ^{0}C. This resulted for the higher density of the samples sintered at 800 ^{0}C for x = 0.2. The highest ion conductivity obtained at a low temperature appeared to be dependent on the structural type (γ - phase) and dopant rate.

Zhang et al. [40] studied the effects of hydrothermal temperature on the synthesis of bismuth vanadate monoclinic structure. It was confirmed that hydrothermal conditions, i.e., time of 16 h and temperature ranging from 140 to 240 ^{0}C, are the favorable for the synthesis of monoclinic bismuth vanadate powders. It was also revealed that this methodology increased the grain size and decreased band gap when hydrothermal temperatures increased.

Zhang et al. [41] studied the $Gd_2O_3/BiVO_4$ composite catalysts which showed monoclinic-$BiVO_4$ structure. It was also seen that the samples displayed enhanced photocatalytic activity when decomposed with metal oxide molecules in aqueous solution. Not only, the morphology and structure type, the electron scavenging effect by Gd^{3+}/ Gd ion-pairs also contributed to the enhanced photocatalytic activity.

Thakaral et al. [42] have studied that the photocatalytic properties of doped $Bi_4V_2O_{11}$ and compared the catalytic activity of bismuth vanadate with other bismuth based photocatalysts studies. They found that the photocatalytic behavior of Al and Gd doped $Bi_4V_2O_{11-\delta}$ for decomposition of Methylene blue (MB) under visible light irradiation was better than the existing bismuth based photocatalysts.

Shangguan et al. [43] examined a series of $Bi_xY_{1-x}VO_4$ mixed oxides (BYV) and found that these solid solutions were proved for the first time to be effective V - based photocatalysts for overall water splitting under UV light irradiation. Under visible light irradiation, BYV solid solutions also performed photocatalytic activity to produce H_2 and O_2 from sacrificial reagent solutions. The optical band gap of BYV mixed oxides tended to decrease with increasing Bi content, and the oxides which contained Bi absorbed visible light. Improvement of photocatalytic activity by incorporation of Bi was ascribed to the interaction between Bi 6s/6p and VO_4^{3-} groups, which caused a reduction of band gap and dispersion of the conduction band. The increasing V – O bond length with the Bi addition from the Raman spectroscopic investigation was considered as a drawback but was treated as a minor factor for photocatalytic activity. Since BYV solid solutions had a rather smaller surface area than usual, the photocatalytic activity was enhanced by increasing the surface area in subsequent research.

Kaur et al. [44] have also studied the structural and optical properties of doped bismuth vanadate. They observed minimum band gap for $Bi_4V_{1.8}Mn_{0.2}O_{11-\delta}$ (~1.7 eV) as compared to $Bi_4V_{1.8}Ga_{0.2}O_{11-\delta}$ (2.04 eV) and $Bi_2V_{1.8}As_{0.2}O_{11-\delta}$ (1.76 eV). The lower value of band gap in $Bi_4V_{1.8}Mn_{0.2}O_{11-\delta}$ is related to the higher contribution of electronic conductivity in this particular system.

Liu et al. [45] explained new visible-light-sensitive hierarchical $Bi_4V_2O_{11}$ hollow microspheres where the Brunauer–Emmett–Teller (BET) surface area of the hollow sample was calculated to be 84.61 m^2g^{-1}, which was much higher than the other prepared $Bi_4V_2O_{11}$ powders. The hierarchical $Bi_4V_2O_{11}$ hollow microspheres exhibited excellent visible light - driven photocatalytic activity for the degradation of Rhodamine-B (RhB). The improved photocatalytic performance was ascribed to the high specific surface area, the narrow band gap and unique hierarchical hollow structure.

CHAPTER 3

EXPERIMENTAL PROCEDURE

3.1 SAMPLE PREPARATION

$Bi_{4-x}Pb_xV_2O_{11-\delta}$ and $Bi_4V_{2-x}Al_xO_{11-\delta}$ ($0.1 \leq x \leq 0.4$) samples were synthesized by solid state reaction by taking stoichiometric amounts of Bi_2O_3, V_2O_5, PbO and Al_2O_3. After mixing the starting powders in acetone media for 1 h to break any agglomerated particles, the mixture is then ball milled for 2 h in order to achieve fully homogeneous mixtures. The resultant mixture was then dehydrated and properly ground. After this, the mixture was calcined to a temperature of 700^0C for 2 h in silica crucibles in the presence of air. The calcined powders were then ground, mixed and refired at 800^0C for 12 h. The resulting powders were again ground and consolidated at a pressure of 12 kN/ cm^2 after mixing with a binder to make pallets of approximately the same dimensions. Next, at 800^0C the prepared pellets were sintered for 10 h.

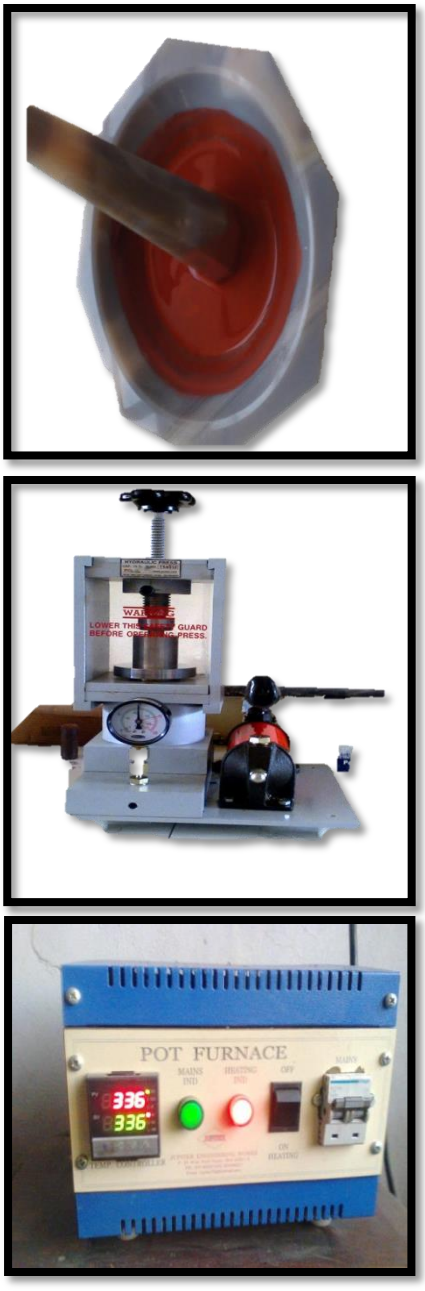

Fig 3.1: Various methods for powder preparation.

3.2 CHARACTERIZATION

The so prepared sintered samples were characterized using X-Ray diffraction (XRD) technique for phase identification by using PANalytical X'Pert PRO system with Ni-filter in the range of $10^0 \leq 2\theta \leq 80^0$. The step size during scan was 0.013^0. The Fourier transform infrared spectroscopy (FT-IR) spectra were obtained by using Perkin Elmer model RZX spectrometer at room temperature in the region 400 - 2000 cm^{-1}. The spectrum of all the samples was normalized to the spectrum of blank KBr. The optical transmission spectra of the samples were recorded using a double beam UV-Vis spectrophotometer (model: Hitachi U-3900H) in the wavelength range of 200 - 600 nm at room temperature. Distilled water was taken as the reference solution. The transmittance spectrum of each sample was normalized to the spectrum of distilled water.

The details of these characterization techniques are given below:

3.2.1 X-RAY DIFFRACTION

X-ray diffraction (XRD) is a powerful technique used to identify the crystalline phases present in the materials and to measure the structural properties (stress, crystal size, strain, and preferred orientation and defect structure) of the phases. XRD is non-contact and non-destructive technique which makes it ideal for the phase identification. When an X-ray beam hits an atom, the electrons start to oscillate with the same frequency as the incoming beam. In all dimensions, we will have destructive interference, i.e., the combining waves are out of phase and there is no resultant energy leaving the solid sample. However, atoms I crystal are arranged in a regular pattern and in a very few directions we will have constructive interference. These waves will be in phase and there will be well-defined X-ray beams leaving the same at various directions.

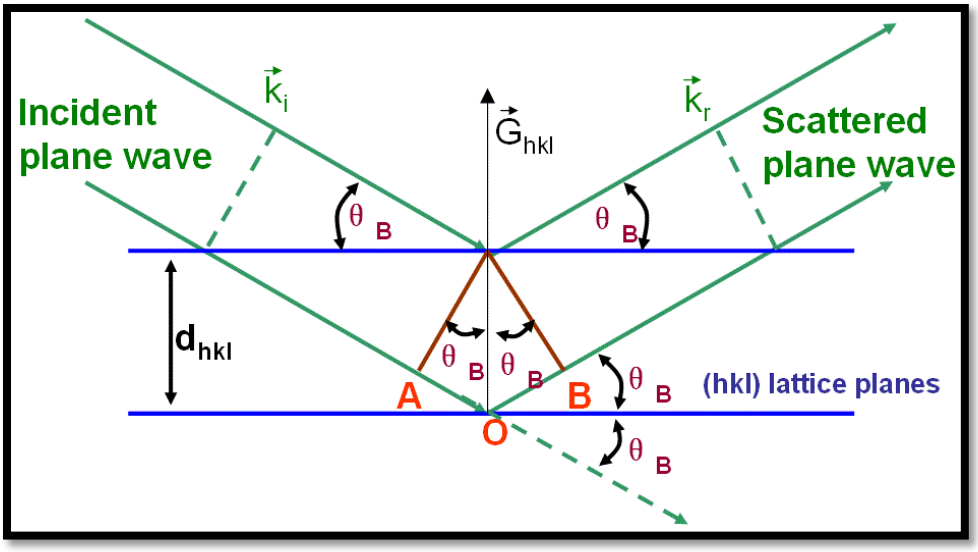

Fig 3.2: The basis of the Bragg's Law [46].

English physicists Bragg and his son developed a relationship in 1913 to explain why the cleavage faces of the crystals appear to reflect X-ray beams at certain angles of incidence which is known as Bragg's Law. The law is given by:

$$n\lambda = 2\,d\sin\theta \qquad (1)$$

The variable *d* is the distance between atomic layers in a crystal, and λ is the wavelength of the incident X-ray beam, n is an integer. This observation is an example of X-ray wave interference (Roentgenstrahlinterferenzen), commonly known as X-ray diffraction (XRD), and was direct evidence for the periodic atomic structure of crystals postulated for several centuries.

Fig 3.3: X-Ray Diffraction set-up.

3.2.1.1 RIETVELD REFINEMENT

It is a standard treatment of powder diffraction data to make the final structural model achieve the accepted criterion. It is the best known method that fully makes use of the step-mode scanned data to dig out a lot of structural and other information.

The model used for describing the powder pattern profile is based in the following expression:

$$y_{ical} = \sum_{\varphi} S_{\varphi} \sum_{h} I_{\varphi h} [ß_I] \Omega (T_i - T_{\varphi h})[ß_P] + B_i[ß_B] \quad (2)$$

Where h labels the Bragg reflections, the subscript f labels the "phase" and varies from 1 up to the number of "phases" existing in the model. W (T_i - $T_{\varphi h}$) is the value of the function Ω(x), normalized to unit area, selected to describe the peak shape, at the position T_i due to the reflection

centered at $T_{\varphi h}$. Finally, S_{φ} is a scale factor and B_i is the background at T_i. In the RM, the functions I [ß$_I$], Ω [ß$_P$] and B [ß$_B$], are calculated using a model that depends on a series of parameters. The structural information is contained in the integrated intensities $I_{\varphi h}$ through the structural parameters [ß$_I$], while the instrumental and microstructural effects are included in the peak shape function which depends on the "profile parameters" [ß$_P$]. The background parameters [ß$_B$] contain information about disorder, short range order, amorphous phases, etc. If the set of model parameters is ß = [ß$_I$] U [ß$_P$] U [ß$_B$] = (ß$_1$, ß$_2$...ß$_P$), where $P = N_I + N_P + N_B$ are the total number free parameters, the Rietveld method tries to optimize the chi-square function:

$$\chi^2_p = \sum_i w_i \{y_{iobs} - y_{ical}(ß)\}^2 \quad (3)$$

Where w_i is the inverse of the variance associated to the observation "i" ($\sigma^2(y_{iobs})$).

The variances of the refined parameters are calculated using the formula:

$$\sigma^2(ß_j) = (A^{-1})_{jj} \chi^2 / (N-P+C) \quad (4)$$

Where A is the matrix of the normal equations and χ^2_n is the reduced chi-square.

3.3.2 FOURIER TRANSFORM INFRARED SPECTROSCOPY (FT-IR)

In infrared spectroscopy, IR radiation is passed through a sample. Some of the infrared radiation is absorbed by the sample and some of it is passed through (transmitted). The resulting spectrum represents the molecular absorption and transmission, creating a molecular fingerprint of the sample. Like a fingerprint no two unique molecular structures produce the same infrared spectrum. This makes infrared spectroscopy useful for several types of analysis.

Fig 3.4: Fourier Transform Infrared Spectroscopy.

Infrared spectroscopy has been a workhorse technique for materials analysis in the laboratory for over seventy years. An infrared spectrum represents a fingerprint of a sample with absorption / transmittance peaks which correspond to the frequencies of vibrations between the bonds of the atoms making up the material. Because each different material is a unique combination of atoms, no two compounds produce the exact same infrared spectrum. Therefore, infrared spectroscopy can result in a positive identification (qualitative analysis) of every different kind of material. In addition, the size of the peaks in the spectrum is a direct indication of the amount of material present. With modern software algorithms, infrared is an excellent tool for quantitative analysis.

The specimen's transmittance and reflectance of the infrared rays at different frequencies is translated into an IR absorption plot consisting of reverse peaks. The resulting FTIR spectral pattern is then analyzed and matched with the known signatures of identified materials in the FTIR library. Our FTIR spectra were obtained by using Perkin Elmer model RZX spectrometer at room temperature in the region 400 - 2000 cm^{-1}.

3.3.3 ULTRAVIOLET AND VISIBLE SPECTROSCOPY

Optical measurements constitute the most important means of determining the band structures of semiconductors. Ultraviolet and Visible Spectroscopy are one the more precious analytical and characterization techniques in determining the optical properties. There is a linear relationship between absorbance and absorber concentration, which makes UV-Vis spectroscopy attractive for making quantitative measurements. In many applications, other techniques could also be used but none is rival UV-Visible Spectroscopy has the characteristics of its accuracy, simplicity, versatility, speed, and cost-effectiveness. This machinery measures the reaction of a sample towards ultraviolet and visible range of electromagnetic radiations. Molecules and atoms show electronic transitions while most of the solids display inter-band transitions in the Ultraviolet and Visible range. Therefore, the energy band gap can be calculated by measuring the absorption of coefficients of molecules.

Now, let the photon beam intensity I_o is incident on the sample of the thickness t and I_t be the intensity of transmitted light. Then,

$$I_t = I_o e^{-\alpha t} \quad (5)$$

And band gap of the samples is calculated by using the following relation:

$$A h \nu = A (h \nu - E_g)^n \quad (6)$$

Fig 3.5: Ultraviolet and Visible Spectroscopy set-up.

Where α is the absorption coefficient, h is Planck's constant, ν if frequency, E_g is optical band gap and n is a constant associated with different types of electronic transitions n = 1/2, 2, 3/2, or 3 for direct allowed, indirect allowed, direct forbidden, and indirect forbidden transitions.

CHAPTER 4

RESULTS AND DISCUSSION

4.1 X-RAY DIFFRACTION

The X-ray diffraction patterns were refined by Rietveld fullproof method. A full profile analysis included a refinement of background, scaling factor, lattice parameters, Bragg peak profile, position and thermal parameters which have been performed for all samples. The overall good agreement between the calculated and calculated patterns is observed for all the samples. The fitted X-ray diffraction patterns of $Bi_{4-x}Pb_xV_2O_{11-\delta}$ and $Bi_4V_{2-x}Al_xO_{11-\delta}$ ($0.1 \leq x \leq 0.4$) are shown in figures 4.1 and 4.2. All the refined parameters are given in tables 4.1 and 4.2.

The fitted XRD patterns confirm that Pb^{2+} doped system exhibits monoclinic structure with C 2/m symmetry. Up to x = 0.2 composition, $Bi_{4-x}Pb_xV_2O_{11-\delta}$ system shows single phase, but after x = 0.2, higher concentration of substituent leads to generation of secondary phase. This secondary phase can be indexed to Bi_2O_3 (ICDD card no 00-001-0709).

The lattice parameters of all the samples are given in table 4.3. The 'b' and 'c' unit cell parameters show a significant change whereas 'a' parameter shows a minor change with substituent concentration. The overall unit cell volume increases with Pb^{2+} concentration in the system. This increase can be attributed to the larger ionic radii of substituent cation Pb^{2+} (1.29 Å) as compared to host cation Bi^{3+} (1.17 Å) [46-48]. Another striking feature observed in this system is that the unit cell volume / lattice parameters show a very slight change up to x = 0.2 concentration and after that this change becomes more significant. This variation can be attributed to the secondary phase which starts appearing after x = 0.2 composition [49].

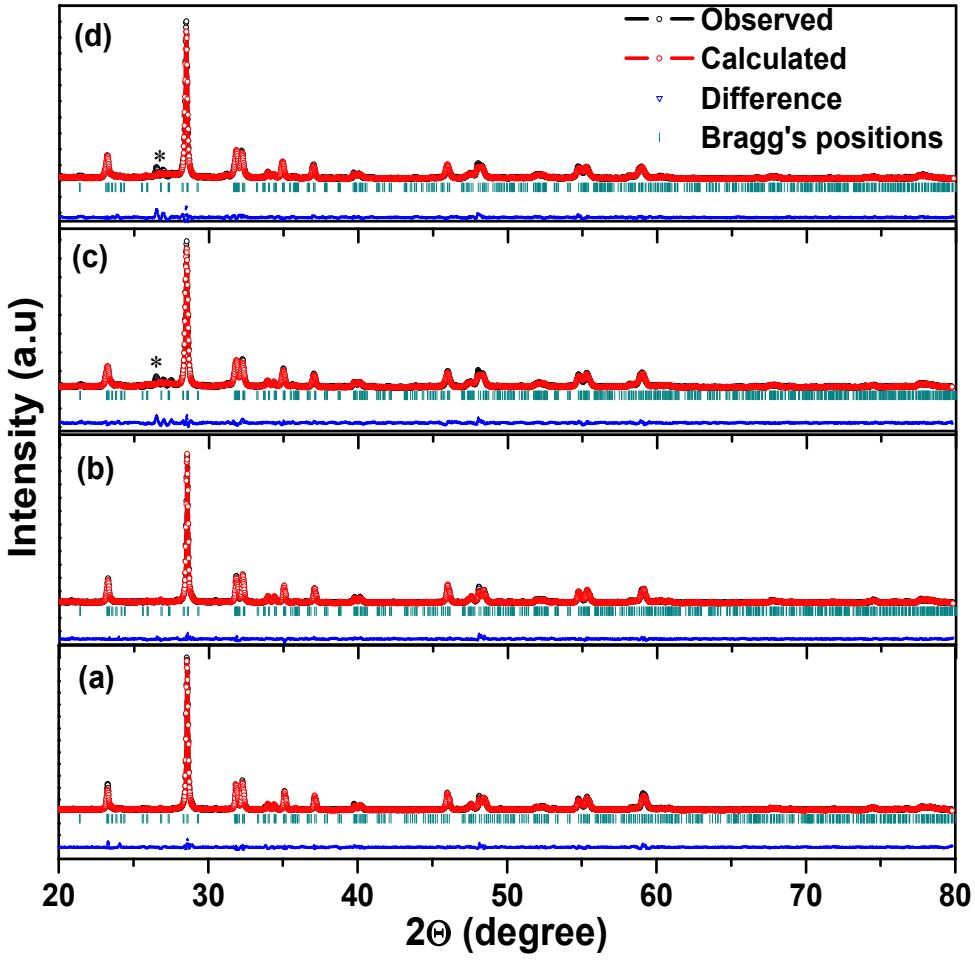

Fig 4.1: Refined X-ray pattern of $Bi_{4-x}Pb_xV_2O_{11-\delta}$ (a) x = 0.1 (b) x = 0.2 (c) x = 0.3 (d) x = 0.4;

****-Bi_2O_3.***

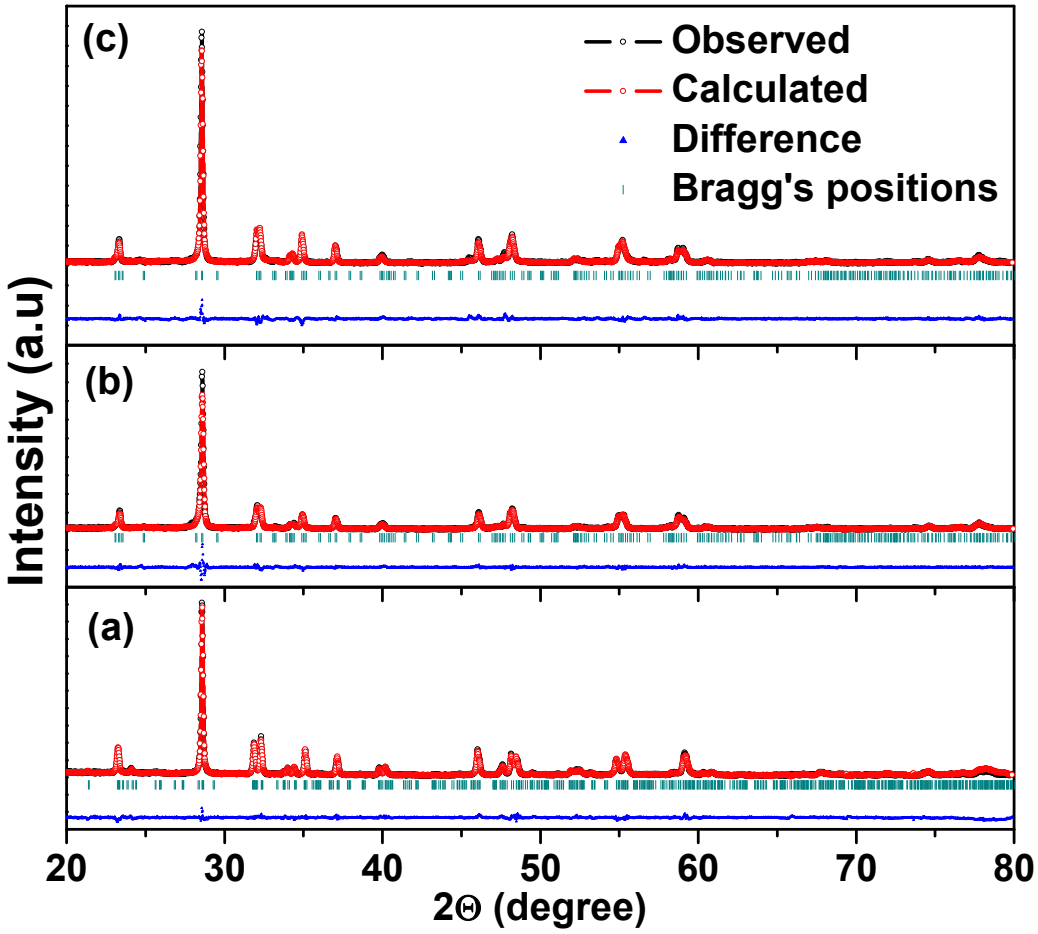

Fig 4.2: Refined X- ray pattern of $Bi_4V_{2-x}Al_xO_{11-\delta}$ (a) x = 0.1 (b) x = 0.3 (c) x = 0.4.

Table 4.1: Structural parameters for C 2/m space group.

Name	*x*	*y*	*z*	*Occupancy*	*Multiplicity*
Bi1	0.00000	0.32601	0.00000	1.00000	4
Bi2	0.98800	0.33121	0.33515	1.00000	8
Bi3	0.00000	0.16831	0.50000	1.00000	4
Bi4	0.03735	0.17125	0.17086	1.00000	8
V1	0.00000	0.00000	0.00000	1.00000	2
V2	0.98490	0.00000	0.34850	1.00000	4
V3	0.55924	0.00000	0.52544	0.50000	4
V4	0.56617	0.00000	0.18278	1.00000	4
O11	0.33874	0.30082	0.14073	1.00000	8
O12	0.24280	0.24098	0.41900	1.00000	8
O13	0.24650	0.24329	0.75346	1.00000	8
O21	0.16379	0.00000	0.25671	1.00000	4
O22	0.30925	0.02100	0.37952	0.50000	8
O23	0.35214	0.00000	0.73808	1.00000	4
O24	0.65403	0.00000	0.11385	1.00000	4
O25	0.72532	0.00000	0.43666	1.00000	4
O26	0.79366	0.22596	0.61118	0.50000	8
O31	0.09200	0.10157	0.70890	0.50000	8
O32	0.56974	0.17297	0.30733	1.00000	8
O33	0.85308	0.39104	0.18672	1.00000	8
O34	0.00000	0.39406	0.50000	1.00000	4

Table 4.2: Structural parameters for Amam space group.

Name	*x*	*y*	*z*	*Occupancy*	*Multiplicity*
Bi(1)	0.00000	0.00000	0.16920	1.00000	8
Bi(2)	0.25000	0.53643	0.16880	1.00000	8
V(1)	0.01920	0.48050	0.00000	0.50000	8
V(2)	0.25000	0.04620	0.00000	1.00000	4
O(1)	0.12218	0.25107	0.24843	1.00000	16
O(2)	0.25000	0.94520	0.10065	1.00000	8
O(31)	0.12520	0.23330	0.00000	1.00000	8
O(32)	0.07410	0.65220	0.06555	0.75000	16

Table 4.3: Lattice parameters of $Bi_{4-x}Pb_xV_2O_{11-\delta}$ and $Bi_4V_{2-x}Al_xO_{11-\delta}$ ($0.1 \leq x \leq 0.4$).

Composition	*a(Å)*	*b(Å)*	*c(Å)*	*β (degrees)*	*R_{wp} (%)*
$Bi_{3.9}Pb_{0.1}V_2O_{11-\delta}$	5.61149(9)	15.3160(2)	16.6094(2)	90.0094(2)	2.96
$Bi_{3.8}Pb_{0.2}V_2O_{11-\delta}$	5.61448(9)	15.3473(2)	16.6199(2)	89.9514(8)	3.45
$Bi_{3.7}Pb_{0.3}V_2O_{11-\delta}$	5.61371(9)	15.3649(2)	16.6305(2)	89.9412(3)	2.56
$Bi_{3.7}Pb_{0.4}V_2O_{11-\delta}$	5.61189(9)	15.3851(2)	16.6421(2)	89.9708(8)	2.34
$Bi_4V_{1.9}Al_{0.1}O_{11-\delta}$	5.6080(3)	15.3161(9)	16.6046(9)	89.953(9)	3.08
$Bi_4V_{1.7}Al_{0.3}O_{11-\delta}$	11.0965(7)	5.5855(3)	15.4110(9)	-	3.15
$Bi_4V_{1.6}Al_{0.4}O_{11-\delta}$	11.0976(8)	5.5865(3)	15.4126(11)	-	2.76

In case of Al^{3+} doped $Bi_4V_{2-x}Al_xO_{11-\delta}$ system, x = 0.1 composition shows the monoclinic structure with C 2/m symmetry whereas compositions above x = 0.1 exhibit orthorhombic structure with Amam symmetry. This change can be due to the increase in vacancy concentration with substitution of Al^{3+} in place of V^{5+} in the lattice. *Joubert et al.* [49] have also reported that substitution of vanadium by subvalent cation at particular concentration leads to an increase in vacancy concentration and stabilization of orthorhombic structure and tetragonal structure. As ionic radii of Al^{3+} and V^{5+} are almost comparable, so, the lattice parameters do not show any remarkable change with increasing substituent concentration.

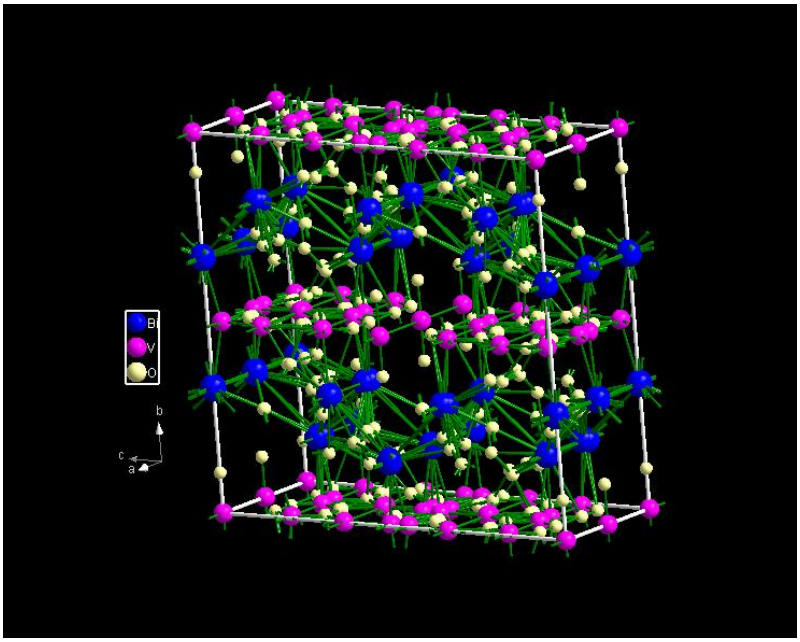

Fig 4.3: Crystal structure of C 2/m space group obtained from refinement.

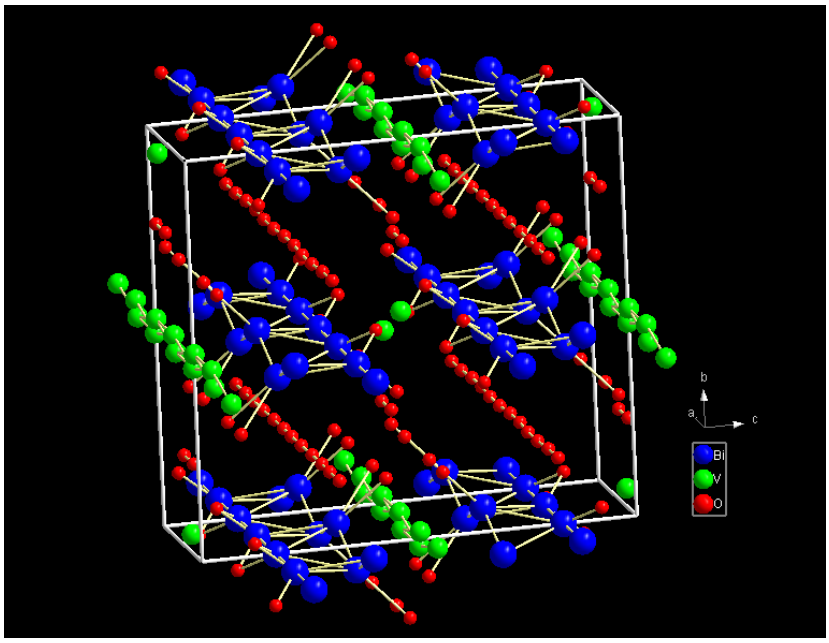

Fig 4.4: Crystal structure of Amam space group obtained from refinement.

4.2 FT-IR Analysis

FT-IR spectra of $Bi_{4-x}Pb_xV_2O_{11-\delta}$ and $Bi_4V_{2-x}Al_xO_{11-\delta}$ ($0.1 \leq x \leq 0.4$) are shown in figures 4.5 and 4.6. In the FT-IR spectra of all studied samples of $Bi_{4-x}Pb_xV_2O_{11-\delta}$ and $Bi_4V_{2-x}Al_xO_{11-\delta}$ ($0.1 \leq x \leq 0.4$); three well known bands at ~520 cm^{-1}, ~620 cm^{-1} and ~790 cm^{-1} are observed. The band around 620 cm^{-1} is assigned mainly to the stretching vibrations of Bi-O bond in BiO_6 octahedral units [50, 51]. The band at ~520 cm^{-1} is also assigned to the stretching vibrations of Bi-O bonds in distorted BiO_6 octahedral units over which longitudinal stretching mode of $V\text{-}O_A$ is superimposed [52-54]. The bands between 770 and 800 cm^{-1} are due to the stretching vibration of $V\text{-}O_A$ [55, 56]. Two strong bands at 1032 and 1082 cm^{-1} are present only in Pb = 0.2 sample. These bands can be attributed to vibration of isolated V=O vanadyl groups in VO_5 trigonal bipyramidal unit [57, 58]. For Al^{3+} doped system, the bands around 500 cm^{-1} can also be assigned to stretching mode of

bonds. Another weak bands observed in x = 0.1 and 0.3 of $Bi_4V_{2-x}Al_xO_{11-\delta}$ at 929 and 465 cm^{-1} can also be due to the Al - O stretching vibrations [59, 60]. In Al doped system, band around 620 cm^{-1} is only found in x = 0.1 after that for higher compositions, it disappears in all the samples. All the assigned vibrations corresponding to each band are tabulated in table 4.4.

In Pb^{2+} doped system, bands around 520 cm^{-1} shifts to higher wavenumber side up to x = 0.1 and after that again shifts to lower wavenumber side. With increasing substituent concentration, bands around 790 cm^{-1} due to vanadyl group shift towards the higher wavenumber side for all the compositions. This suggests that the presence of Pb^{2+} cation influences the surrounding of Bi^{3+} cations which further influence the $V\text{-}O_4$ units and BiO_6 octahedral units [61].

Table 4.4: Infrared absorption bands and their detailed assignments.

Wavenumber (cm^{-1})	***Band Assignment***
510-520	Bi-O bonds in [BiO_6] structural units
610-620	Bi-O bonds of different lengths in the distorted BiO_6 polyhedra
450-500, 950	Symmetric stretching vibration of Al-O bonds
720-780, 800-830	V-O-V symmetric stretching
1032, 1081	Stretching vibration of V-O

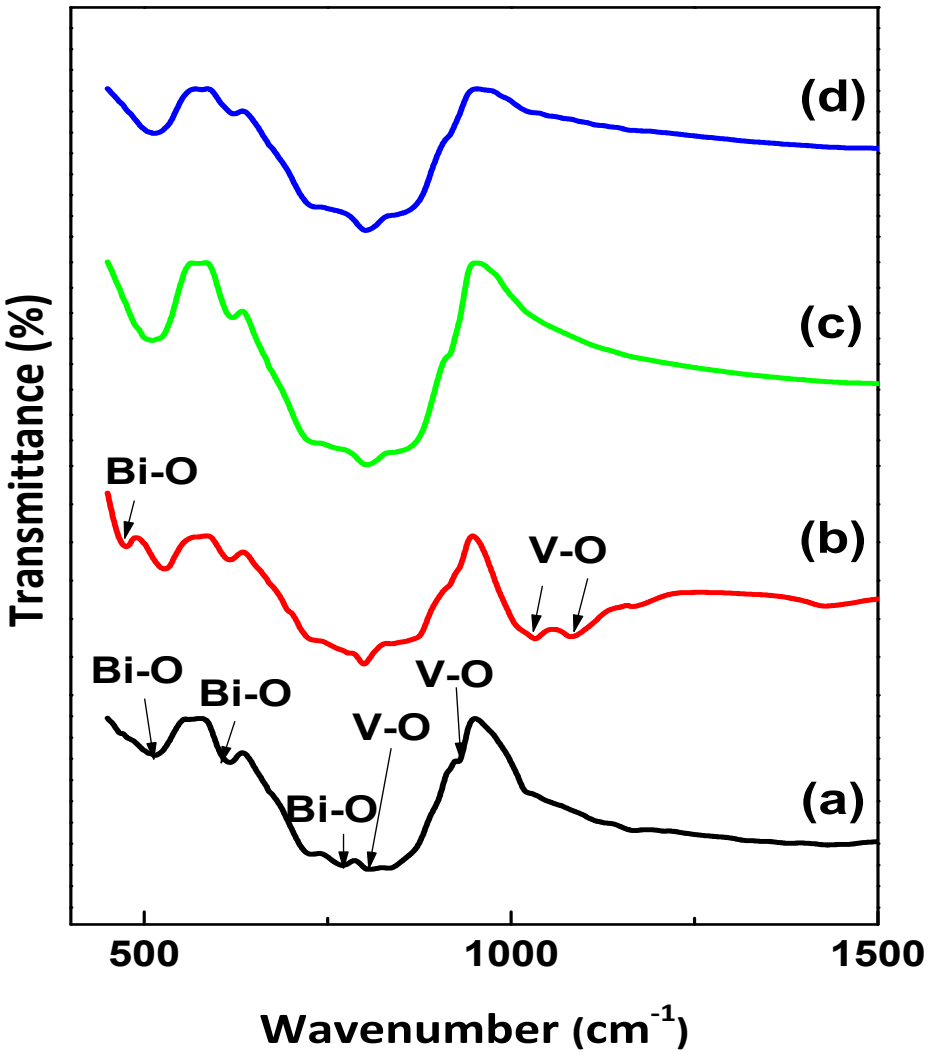

Fig 4.5: FT-IR spectra of $Bi_{4-x}Pb_xV_2O_{11-\delta}$ (a) x = 0.1 (b) x = 0.2 (c) x = 0.3 (d) x = 0.4.

As compared to Pb^{2+} substituted system, more bands related to vanadyl group are observed in Al^{3+} substituted system. Whereas, the reverse trend is observed for Bi-O vibrations bands. The shifting of the bands towards either side of wavenumber is also more prominent in Al^{3+} substituted system. This difference can be due to the different substituent cations size and their different occupancy sites in the lattice for both the systems. As the substitution on the vanadium sites will

create more oxygen disordering in the system, so, that is why changes are more prominent in Al^{3+} substituted system as compared to Pb^{2+} substituted system.

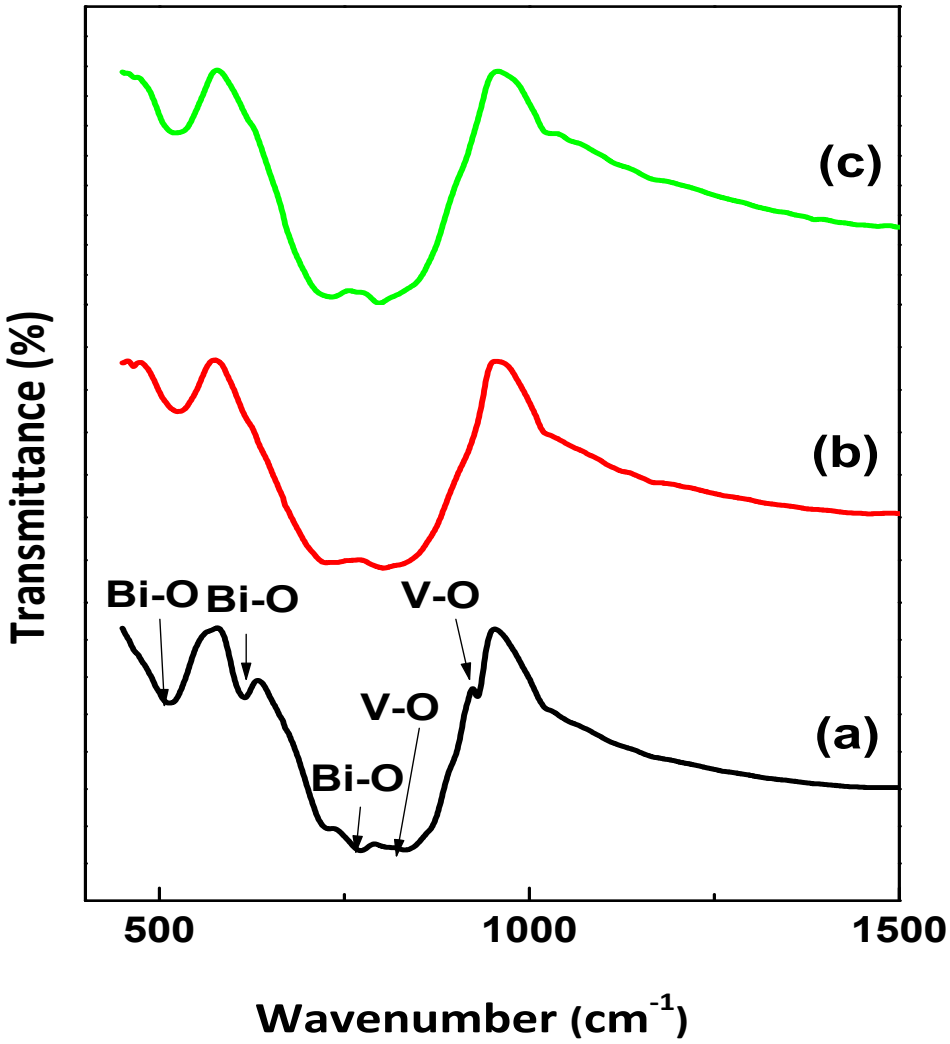

Fig 4.6: FT-IR spectra of $Bi_4V_{2-x}Al_xO_{11-\delta}$ (a) x = 0.1 (b) x = 0.3 (c) x = 0.4.

In Al^{3+} doped system, the major effect is on the bands around 770-830 and 520 cm^{-1}. The band around 520 cm^{-1} which is due to the Al-O and vanadyl group shifts towards higher wavenumber side where as band around 770-830 cm^{-1} due to the vanadyl group shifts towards lower

wavenumber side with increasing substituent concentration. This can be due to the increasing occupancy of vanadium site with substituent atom as the substituent concentration increases.

4.3 ANALYSIS OF UV-VISIBLE SPECTRA

According to Wood and Tauc, the absorbance, photon energy and band gap are related by the equation [62]:

$$\alpha h\upsilon = A\,(h\upsilon - E_g)^n \qquad (7)$$

Where, α is absorbance, h is planck's constant, υ is frequency, E_g is the optical band gap and n is a constant associated to different types of electronic transitions (n= 1/2, 2, 3/2 or 3 for direct allowed, indirect allowed, direct forbidden and indirect forbidden transitions, respectively. The variation of $(\alpha h\upsilon)^2$ with respect to $h\upsilon$ are shown for Pb^{2+} substituted samples in figure 4.7 and for Al^{3+} substituted samples in figure 4.8. The optical band gap energies are obtained by extrapolation of linear region of curves to hυ axis i.e. $(\alpha h\upsilon)^2$ =0. The values of optical band gap are given in table 4.5.

The band gap of pure $Bi_4V_2O_{11-\delta}$ is reported around 2.5 eV [63]. The low band gap values of the substituted system as compared to pure system can be attributed to the structural changes arising due to occupancy of different substituent at different sites in the lattice. In Pb^{2+} substituted system, the optical energy band gap values decreases up to x = 0.2 composition and after that again starts increasing. The decrease in optical band gap energy values may be due to the increasing defects concentration with substituent concentration and after x = 0.2, increases in these values can be due to the increasing secondary phase. For Al^{3+} substituted system, these

values show continuous decrease with increasing substituent concentration. This decrease can be due to the increase in defects and disordering in oxygen vacancies as supported by the XRD and FT-IR results. The Al^{3+} substituted system shows lower band gap values as compared to Pb^{2+} doped system. This change can be due to the different occupancy sites of these cations in pure system. This difference between two substituents can also be explained as: the valence band of $Bi_4V_2O_{11-\delta}$ is suggested to be composed of Bi 6s orbitals and oxygen 2p orbitals whereas the conduction band consists of V 3d orbitals. In the case of Pb^{2+} doped system, the valence band will also have Pb^{2+} 6s orbitals and for Al^{3+} system , the conduction band will consist of aluminium 3s orbitals along with V 3d orbitals. Due to different orbital symmetry of aluminium and vanadium strong interaction between the orbitals is expected which will further perturb the conduction band and will lower the band gap values. This effect will be low in case of lead substituted system as both bismuth and lead have almost same orbital symmetry [64].

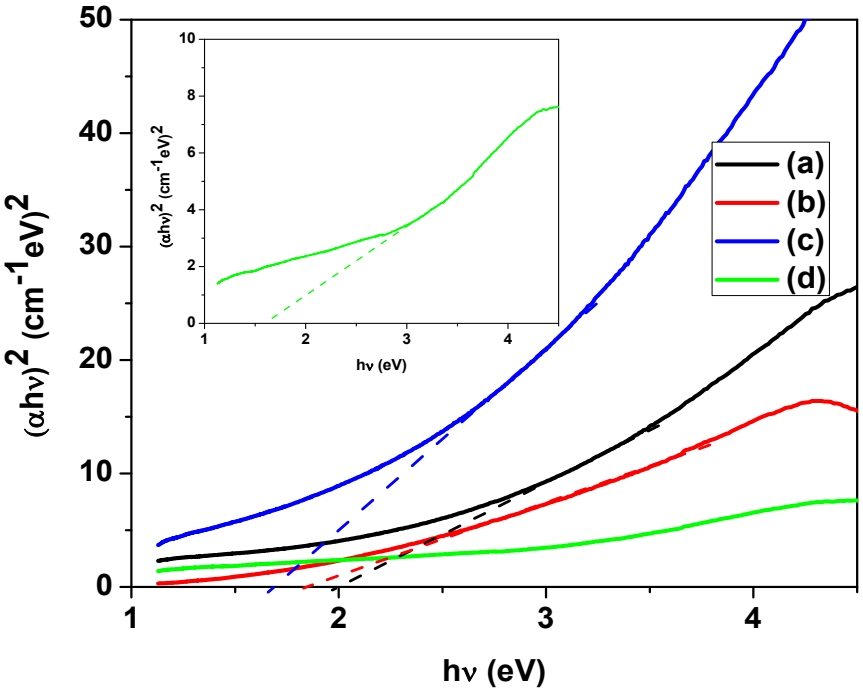

Fig 4.7: UV-visible spectra of $Bi_{4-x}Pb_xV_2O_{11-\delta}$ (a) x = 0.1 (b) x = 0.2 (c) x = 0.3 (d) x = 0.4.

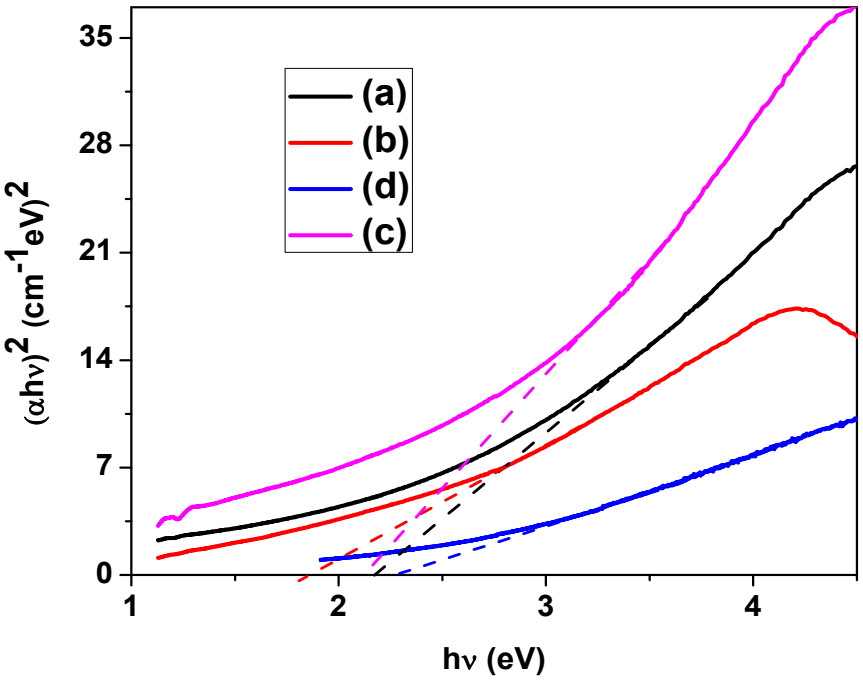

Fig 4.8: UV-visible spectra of spectra of $Bi_4V_{2-x}Al_xO_{11-\delta}$ (a) x = 0.1 (b) x = 0.3 (c) x = 0.4.

The defects in the system can be correlated to the Urbach energy. The relation between the Urbach energy (E_u) and absorption coefficient (α (υ)) is given by empirical Urbach law as [65]:

$$\text{Ln}\,\alpha = \frac{h\upsilon}{E_u} + \text{Constant} \qquad (8)$$

The value of the Urbach energy is calculated from the slope of linear portion of the curve between ln α and hυ which is given in table 4.5. The Urbach energy is an empirical parameter having dimensions of energy and describes the width of localized states in the band gap. The origin of the exponential absorption is generally related to the random fluctuations in the potential associated with any lattice absorptions like thermal vibrations, dislocations, electric fields of defects which can further affect the energy bands and cause tailing of energy states into forbidden gap [66].

In the Pb^{2+} substituted system, Urbach energy increases up to after x = 0.2. After that due to the presence of the secondary phase, the band gap increases and Urbach energy decreases. For Al^{3+} doped samples, Urbach energy increases with increasing substituent concentration and decreasing band gap values. The materials with large Urbach energy values will have a great tendency to generate defects and therefore will have low optical energy band gap values. This fact is well obeyed in the present system.

Table 4.5: The optical band gap energy (in eV) and Urbach energy (in eV) of $Bi_{4-x}Pb_xV_2O_{11-\delta}$ and $Bi_4V_{2-x}Al_xO_{11-\delta}$ ($0.1 \leq x \leq 0.4$).

Composition	***x = 0.1***		***x = 0.2***		***x = 0.3***		***x = 0.4***	
	E_g	E_u	E_g	E_u	E_g	E_u	E_g	E_u
$Bi_{4-x}Pb_xV_2O_{11-\delta}$	2.09	0.45	1.94	0.54	2.10	0.51	2.18	0.49
$Bi_4V_{1-x}Al_xO_{11-\delta}$	2.01	0.47	1.77	0.50	1.69	0.53	1.66	0.55

CONCLUSION

The present study was carried out to evaluate the effect of two different dopants on structural and optical properties of $Bi_4V_2O_{11-\delta}$. The two different cations Pb^{2+} and Al^{3+} are doped with different concentrations on Bi^{3+} and V^{5+} sites and their effect on different properties has been discussed. The Rietveld refinement confirms that $Bi_{4-x}V_2O_{11-\delta}$ ($0.1 \leq x \leq 0.4$) and $Bi_4V_{1.9}Pb_{0.1}O_{11-\delta}$ exhibit monoclinic structure with C 2/m symmetry whereas, above x = 0.1 substituent concentration aluminum doped system has orthorhombic structure with Amam symmetry. The samples of Pb doped system show secondary phase above x = 0.3 compositions, in contrary to this, all the aluminum doped samples of studied range are single phase. From XRD and FT-IR patterns, it can be concluded that Al^{3+} substituted system have more oxygen vacancy concentration as compared to Pb^{2+} doped system. This disordering also leads to lower optical band gap values and higher Urbach energy values of Al^{3+} system as compared to Pb^{2+} substituted system. With the increase in substituent concentration, disordering increases with increase in Urbach energy and decrease in optical band gap values. The band gap values of all the samples lie in the semiconducting range. The lowest band gap of 1.66 eV is observed for $Bi_4V_{1.6}Al_{0.4}O_{11-\delta}$ among all the studied samples.

FUTURE SCOPE

After analyzing the data, the following suggestions are recommended for further investigations: Study of defect chemistry will help for the detailed analysis of oxygen vacancies, and their vacancies on ionic conductivity and band gap values of the present studied samples. Further, the effect of two different dopants on dielectric and ferroelectric properties of these samples can also be investigated. Particularly, high concentration of Al^{3+} dopant should be investigated to know the solid solution limit of the dopants. To obtain the proper correlation between dopants and morphology, scanning electron microscopy investigation can also be carried out on the present systems.

REFRENCES

[1] JC Boivin, C Pirovano, G Nowogrocki, G Mairesse, P Labrune, G Lagrange, Solid State Ionics, 1998, 639, 113.

[2] C Pirovano, RN Vannier, E Capoen, G Nowogrocki, M Anne, JC Boivin, G Mairesse, TA Ramanarayanan, WL Worrell, M Mogensen, Proceedings of the Ionic and Mixed Conducting Ceramics IV, San Francisco, The Electrochemical Society, 2001, 339.

[3] JB Goodenough, A Manthiram, M Paranthamam, YS Zhen, Mater Sci Eng B 1992, 12, 357.

[4] JR Dygas, F Krok, W Bogusz, P Kurek, K Reiselhuber, F Breiter, Solid State Ionics, 1994, 239, 70.

[5] P Kurek, JR Dygas, F Breiter, J Electroanal Chem, 1994, 378, 77.

[6] F Abraham, JC Boivin, G Mairesse, G Nowogrocki, Solid State Ionics 1990, 529, 40.

[7] A Patil, V Patil, DW Shin, JW Choi, DS Paik, SJ Yoon, Materials Research Bulletin**,** 2008, 43, 1913.

[8] J Jirmann, International Journal of Infrared and Millimeter Waves, 1985, 6, 1091.

[9] L Rengui, F Zhang, D Wang, J Yang, M Li, J Zhu, X Zhou, H Han and C Li, Nature Communications, 2013, 4, 1.

[10] M Huve, RN Vannier, G Nowogrocki, G Mairesse, G Van Tendeloo, J. Mater. Chem., 2000, 10, 2811.

[11] F Abraham, MF Debreuille-Gresse, G Mairesse, G Nowogrocki, Solid State Ion., 1988, 529, 28.

[12] B Aurivillius, Ark Kemi., 1949, 1, 463.

[13] B Aurivillius, Ark Kemi., 1949, 1, 499.

[14] I Abrahams, F Kork, J. Mater. Chem., 2002, 12, 3351.

[15] B Frit, JP Mercurio, J. Alloys Comp., 1992, 188, 27.

[16] G Mairesse, P Roussel, RN Vannier, M Anne, G Nowogrocki, Solid State Sciences, 2003, 5, 861.

[17] T Kikuchi, Mater. Res. Bull., 1979, 14, 1561.

[18] H Tezuka, M Kato, T Kajita, T Noji, Y Koike, Physica C: Superconductivity, 2008, 468, 1152.

[19] O Joubert, A Jaouanneaux, M Ganne, Mater Res Bull, 1994, 29, 175.

[20] G Mairesse, B Scrosati, A Magistris, CM Mari, G Mariotto, Kluwer Academic Publishing, Dordreckt, 1995, 85, 271.

[21] F Abraham, JC Boivin, G Mairesse, G Nowogrocki, Solid State Ionics, 1990, 934, 40.

[22] M Huvé, RN Vannier, G Nowogrocki, G Mairesse, G Van Tandeloo, J. Mater. Chem., 1996, 6, 1339.

[23] RN Vannier, G Mairesse, F Abraham, G Nowogrocki, E Pernot, M Anne, M Bacmann, P Strobel, J Fouletier, Solid State Ionics, 1995, 78, 183.

[24] M Guillodo, J Fouletier, L Dessemond, PD Gallo, Journal of the European Ceramic Society, 2001, 21, 2331.

[25] Y Nemirovsky, A Nemirovsky, P Muralt, N Setter, Sens. Actuators A, 1996, 56, 239.

[26] O Joubert, A Jaouanneaux, Mater Res Bull, 1993, 29, 175.

[27] KVR Prasad, KBR Varma, Active and Passive Elec. Comp., 1995, 18, 137.

[28] KVR Prasad, KBR Varma, Materials Chemistry and Physics, 1994, 38, 406.

[29] SK Ramaesha, KVR Prasad, MV Shankar, KBR Varma, Advances in High Pressure Science B Technology, 1994.

[30] KVR Prasad, KBR Varma, AR Raju, Journal of Materials Science 1994, 29, 2691.

[31] K Shantha, KBR Varma, Solid State Ionics, 1995, 99, 225.

[32] W Zhou, DA Jefferson, H He, J Yuan, DJ Smith, Philosophical Magazine Letters, 1997, 75, 105.

[33] I Abrahams, AJ Bush, F Krok, GE Hawkes, KD Sales, P Thorntona, W Boguszb, J. Mater. Chem., 1998, 8, 1213.

[34] F Xia, X Yao, Fermelectrics, 1999, 231, 121.

[35] M Joseph, HY Lee, H Tabata, T Kawai, Journal of Applied Physics, 2000, 88, 2.

[36] RN Vannier, E Pernot, M Anne, O Isnard, G Nowogrocki, G Mairesse, Solid State Ionics, 2003, 157, 147.

[37] R Kant, K Singh, OP Pandey, International Journal of Hydrogen Energy, 2008, 33, 455.

[38] N Kumari, SB Krupanidhi, KBR Varma, Materials Science and Engineering B, 2007, 138, 22.

[39] R Kant, K Singh, OP Pandey, International Journal of Hydrogen Energy, 2008, 33, 455.

[40] A Zhang, J Zhang, Materials Science-Poland, 2009, 1015.

[41] A Zhang, J Zhang, J Mater Sci, 2010, 4040.

[42] V Thakral, S Uma, Materials Research Bulletin, 2010, 45, 1250.

[43] H Liu, J Yuan, Z Jiang, W Shangguan, H Einagac, Y Teraoka, J. Mater. Chem., 2011, 21, 16535.

[44] G Kaur, OP Pandey, K Singh, Physica status solidi A, 2012, 209, 1231.

[45] X Chen, J Liu, H Wang, Y Ding, Y Suna, H Yana, J. Mater. Chem. A, 2013, 1, 877.

[46] V Raghvan, Material Science and Engineering, PHI Learning Private Limited, New Delhi, 2010.

[47] H Tuller, J Schoonman, I Riess, NATO ASI (Kluwer,Dordrecht), 2000, 245.

[48] R Kant, OP Pandey, K Singh, Mater. Sci. Eng. B, 2009, 158, 63.

[49] R Kant, OP Pandey, K Singh, Physica Status Solidii A, 2010, 207, 321.

[50] O Joubert, M Ganne, RN Vannier, G Mairesse, Solid State Ionics, 1996, 83, 199.

[51] R Punia, RS Kundu, J Hooda, S Dhankhar, S Dahiya, NJ Kishore, Appl. Phys., 2011, 110, 0335271.

[52] FH ElBatal, MA Marzouk, AM Abdelghany, J Mater Sci, 2011, 46, 5140.

[53] SS Rojas, JED Souza, MRB Andreeta, AC Hernandes, J. Non-Cryst. Solids, 2010, 356, 2942.

[54] ASI Urca, B Orel, Electrochimica Acta, 1999, 44, 3051.

[55] FH ElBatal, MA Marzouk, AM Abdelghany, J. Non-Cryst. Solids, 2010, 357, 1027.

[56] A. A. El-Moneim, Mater. Chem. Phys. 2002, 73, 318.

[57] V Dimitrov, A Montenero, J. Non-Cryst. Solids 1994, 51, 180.

[58] D Manara, A Grandjean, O Pinet, JL Dussossoy, DR Neuville, J. Non-Cryst. Solid, 2007, 353, 12.

[59] S Rada, E Culea, V Rus, M Pica, M Culea, J. Mater. Sci., 2008, 43, 3713.

[60] TMH Costa, MR Gallas, EV. Benvenutti, JAH da Jornada, J. Phys. Chem. B, 1999, 103, 4278.

[61] D Goldstein, JA McCormick, SM George, J. Phys. Chem. C, 2008, 112, 19530.

[62] E Araceli, A Ravat, J Enrique, J Baran, J. Alloys and Compounds, 2008, 460, 152.

[63] J Tauc, Mater.Res. Bull., 1970, 5, 721.

[64] F Urbach, Phys. Rev., 1953, 92, 1324.

[65] S Sebastian, MS Khadar, Bull. Mater. Sci., 2004, 27, 2007.

[66] E Mansour, KE Egili, GE Damrawi, Phys. Rev. B, 2007, 392, 221.